Effect of salt on the H-bond symmetrization in ice

Livia Eleonora Bove[a,b,1], Richard Gaal[b], Zamaan Raza[a,c], Adriaan-Alexander Ludl[a], Stefan Klotz[a], Antonino Marco Saitta[a], Alexander F. Goncharov[d], and Philippe Gillet[b]

[a]Institut de Minéralogie, de Physique des Matériaux et de Cosmochimie, CNRS UMR 7590, Université Pierre et Marie Curie, F-75252 Paris, France; [b]Institute of Condensed Matter Physics, Ecole Polytechnique Federal de Lausanne, CH-1015 Lausanne, Switzerland; [c]Department of Physics, Chemistry and Biology, Linköping University, SE-581 83 Linkoping, Sweden; and [d]Geophysical Laboratory, Carnegie Institution of Washington, Washington, DC 20015

Edited by Frank H. Stillinger, Princeton University, Princeton, NJ, and approved May 27, 2015 (received for review February 5, 2015)

The richness of the phase diagram of water reduces drastically at very high pressures where only two molecular phases, proton-disordered ice VII and proton-ordered ice VIII, are known. Both phases transform to the centered hydrogen bond atomic phase ice X above about 60 GPa, i.e., at pressures experienced in the interior of large ice bodies in the universe, such as Saturn and Neptune, where nonmolecular ice is thought to be the most abundant phase of water. In this work, we investigate, by Raman spectroscopy up to megabar pressures and ab initio simulations, how the transformation of ice VII in ice X is affected by the presence of salt inclusions in the ice lattice. Considerable amounts of salt can be included in ice VII structure under pressure via rock–ice interaction at depth and processes occurring during planetary accretion. Our study reveals that the presence of salt hinders proton order and hydrogen bond symmetrization, and pushes ice VII to ice X transformation to higher and higher pressures as the concentration of salt is increased.

salty ices | extreme conditions | ice bodies | H-bond symmetrization | proton quantum effects

All models of the interior of ice bodies in the universe rely on our knowledge of the behavior of a few simple molecules under high pressure and temperature (1–22), water being the most intriguing of them, due to its abundance and its connection to life existence.

New data delivered by various space missions, such as the Voyager, Galileo, and Cassini–Huygens missions, have greatly improved our understanding of the icy bodies within the solar system (23–25), and recent discoveries of extrasolar planets with significant water ice content have highlighted the importance of high-pressure H_2O-rich phases in planetary physics beyond the solar system (26).

Water displays an unusually rich pressure–temperature phase diagram, which mainly derives from the open geometry of the water molecule, which favors tetrahedral arrangements, and from the possibility of configurational disorder of the protons in the lattice. However, at high pressure (above about 2 GPa), the system experiences a large densification as a result of the interpenetration of low-pressure structures, and only two molecular phases are known, ice VIII and VII (3, 4). Ice VII is composed of two interpenetrating but not interconnected tetrahedral hydrogen-bonded networks of water molecules of normal cubic ice, Ic, with a body-centered-cubic (bcc) oxygen structure. The orientation of the water molecules is disordered, resulting in a paraelectric phase. In the antiferroelectric ice VIII phase, the water molecules and the associated dipole moments on the two sublattices possess long-range order and point in opposite directions, promoting a slight tetragonal distortion of the cubic unit cell along the staggered polarization (3, 4). In these two phases, the hydrogen bonds are characterized by a pronounced double-well proton transfer potential. Upon reducing the distance between donor and acceptor oxygens, the proton potential degenerates into a single-well potential (27–31), giving rise to a symmetric or centered hydrogen bond, where hydrogen atoms are located midway between two neighboring oxygen atoms. Infrared (IR), Raman, and X-ray measurements (5–10) have provided evidence for the transition in water from the molecular proton-disordered ice VII to an atomic phase with symmetric hydrogen bonds when the distance between acceptor and donor oxygen atoms decreases below 2.3 Å (at about 60 GPa).

Quantum effects play an essential role in the phenomenon of hydrogen bond centering; thus the description of ice VII and ice VIII transformation to the atomic ice X represents a stringent benchmark for theoretical calculations (27–35). First-principle calculations predict an intricate pretransitional behavior characterized by possible intermediate disordered ice X or VII phases (27–30, 35). At room temperature, this transition is described as a change from frozen-in static disorder to dynamical disorder mainly induced by proton hopping along hydrogen bonds, via transient ionic defects (27). However, while it is well known that the number of ionic defects in ice can be remarkably increased by salt dissolution in water (36), the effect of dissolved ions on ice VII to ice X transition has never been investigated.

Recently, unexpected evidence has emerged that high-pressure water polymorphs can contain a substantial amount of small ions in salty ice structures (37–42), and, similarly to what is observed in ice clathrates (43, 44), they transform under pressure into bcc O lattices with ions either occupying interstices (37) or being substitutional to water molecules (37, 39). These "filled" ice structures can be stable over several gigapascals and hundreds of Kelvins, conditions encountered in large ice bodies in the universe. Combined neutron scattering experiments and molecular dynamics simulations have allowed sketching of the pressure and Temperature (p-T) phase diagram of LiCl–water and NaCl–water mixtures up to a few gigapascals, and have shown that the presence of salt suppresses the ordered ice VIII phase and modifies the boundary of the proton-disordered ice VII phase (37–42). Orientational disorder of water molecules is also enhanced by the presence of salt, as demonstrated by the

Significance

Ice-VII and ice-X phases are the most stable forms of ice at high temperature and extreme pressures, typical of the interiors of satellites and planets. The phase transition between them is a prototypical case of quantum-driven phenomenon, as it can be described as a quantum delocalization of protons in the middle of O–O distances. In this study, we investigate the effect of ions on such quantum effects. We show that the presence of ions significantly modifies the fundamental H-bond properties of water ices. This finding could challenge our present description of the physics of ice bodies, essentially based on the assumption of the properties of pure ice under high pressure.

Author contributions: L.E.B., S.K., and P.G. designed research; L.E.B., R.G., Z.R., A.-A.L., S.K., A.M.S., and A.F.G. performed research; R.G. and A.M.S. contributed new reagents/analytic tools; L.E.B., R.G., and A.F.G. analyzed data; and L.E.B. wrote the paper.

The authors declare no conflict of interest.

This article is a PNAS Direct Submission.

Freely available online through the PNAS open access option.

[1]To whom correspondence should be addressed. Email: livia.bove@impmc.jussieu.fr.

This article contains supporting information online at www.pnas.org/lookup/suppl/doi:10.1073/pnas.1502438112/-/DCSupplemental.

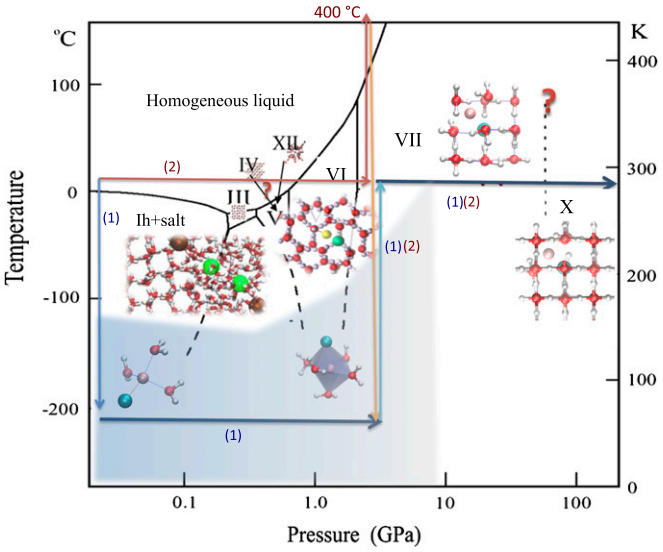

Fig. 1. Pressure–temperature phase diagram of salty ice as sketched from our previous neutron diffraction experiments and MD simulations on LiCl–water solutions under pressure (37, 38, 49). In the present experiment, we probed the ice VII to ice X transition, both in compression and decompression, in the 10- to 150-GPa range and room temperature by Raman scattering. Specific thermodynamics paths have been followed for $R = 6$ and 12 solutions (path 1) and for $R = 30$ and 50 solutions (path 2) to first produce the amorphous precursor embedding the salt and then crystallize salty ice under pressure (37). The shadowed part is the region of existence of the polyamorphic phases (38).

calculated water dipolar momentum distribution (37), and plastic phases are likely promoted in salty ices at lower temperature then predicted in pure ice (45, 46). The existence of high-pressure symmetric phases in the presence of ionic impurities was not investigated in these studies, due to the pressure limitations of neutron diffraction technique.

Results

In this paper, we report on a Raman study up to megabar pressures of ice phases containing LiCl at different concentrations. LiCl–water is a model system used since the early 1970s in several seminal studies investigating the effect of salts on water structure (47, 48). Due to its high vitrification ability, LiCl–water also represents the ideal system to produce the salty amorphous ice phases serving as precursors for salty ice VII crystallization under pressure (37–39) (details are given in *Sample Preparation*). Despite a different ability to vitrify (47–49) and to undergo polyamorphic transitions at ambient and moderate pressures (39), LiCl and more naturally abundant NaCl produce very similar modifications on water structure and equations of state at high pressure (39–42).

The explored pressure range, 2–150 GPa, covers the stability fields of ice VII, ice VIII, and ice X phases in pure water. Raman spectroscopy coupled with the diamond anvil cell technique is ideal for probing hydrogen bond symmetrization. In particular, the observation of a single O–O vibrational mode of T_{2g} symmetry in the low-frequency range (5, 6) is commonly used to identify the transition to the cuprite-type structure of ice X. A sketch of the high-pressure phase diagram of salty LiCl water so far known (37, 38, 41, 49) is represented in Fig. 1, where the thermodynamic paths followed in the present experiment are also indicated.

Salty ice VII samples $LiCl:RH_2O$, where R indicates the water molecules/salt ratio, at different salt concentrations $R = 6$ (15 mol%), $R = 12$ (8 mol%), $R = 30$ (3.5 mol%), and $R = 50$ (2% mol) were prepared following the procedure detailed in *Methods* and depicted in Fig. 1.

All of the samples have been first characterized at low pressure, where a significant broadening of the lineshape of the OH stretching modes with respect to pure ice H_2O is observed (see *Supporting Information*), as expected in the presence of interstitial impurities. Subsequently, they have been slowly compressed at room temperature up to 120–150 GPa, with pressure steps of the order of 10 GPa, to monitor the ice VII to ice X transformation. In particular, the softening of the OH stretching modes with pressure and the appearance of the characteristic ice X O–O T_{2g} mode have been measured at high resolution and compared with a pure H_2O sample (*Methods*).

The high-frequency OH stretching vibrations in H_2O ice VII form a disorder-broadened triplet, assigned to ν_1 (A_{1g}), ν_3 (E_g), and ν_1 (B_{1g}) modes in order of increasing frequency. As in refs. 5–7, we observe softening of these modes with pressure, signaling the approach of displacive phase transitions. Despite the merging with the second-order band from the diamond anvils in the pressure range of 30–50 GPa, depending on salt concentration, we were still able to track the behavior of these bands up to 50 GPa by subtracting the signal from the stressed diamond anvil in contact with the gasket measured at each pressure point (for further details, see *Supporting Information*). Above this pressure, the subtraction is, in our opinion, no more reliable as the three modes decrease in intensity and become much weaker than the diamond background. The high-frequency ν_1 (A_{1g}) band has the largest pressure shift in pure water, and its softening has been directly linked to the appearance of the ice VII to ice X transition (5, 6) at higher pressures. It can be readily observed from Fig. 2 that the softening of these bands is strongly reduced by the presence of salt.

Further increase of pressure to about 80 GPa results in the appearance of a new, narrow band in the low-frequency spectrum,

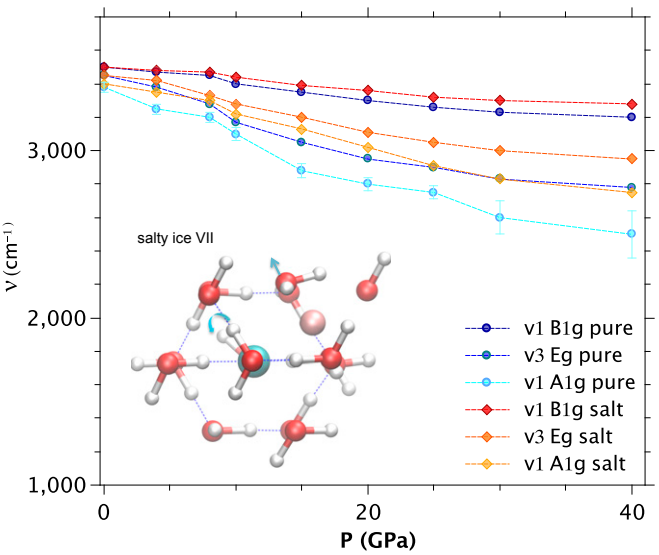

Fig. 2. Raman frequencies of ν_1 (A_{1g}), ν_3 (E_g), and ν_1(B_{1g}) modes as a function of pressure in pure H_2O compared with $LiCl{:}12H_2O$ up to 40 GPa. For higher pressures, the triplet strongly decreases in intensity, and at $P = 50$ GPa, it merges into the second-order Raman signal from the diamond anvils, hindering a reliable quantitative analysis of the peak shifts. The pressure dependence of the OH stretch Raman bands in pure ice VII are in agreement with previous high-pressure Raman measurements (5, 6). Solid lines are guides to the eye. (*Inset*) A simulation snapshot of salty ice VII structure, where the Cl ion substituting a water molecule is represented in blue and the interstitial Li ion is in pink. The water orientational distortion and the O displacement close to the ions can be readily observed.

PHYSICS

attributed to the O–O stretching mode in the symmetric ice X phase (5, 6). The frequency of this new excitation increases with pressure, and the corresponding peak is the only first-order excitation in pure H_2O at these pressures, due to symmetry restrictions (5–9). As shown in Fig. 3, the appearance of this band is pushed to higher pressures (namely at about 90 GPa, 100 GPa, and 120 GPa for $R = 50$, 30, and 12 solutions, respectively) in the presence of salt inclusion. Furthermore, the presence of the O–O stretching mode was not observed in the $R = 6$ salt solutions up to the maximum investigated pressure, $P = 145$ GPa.

Ab initio computer simulations were performed on a $3 \times 3 \times 3$ supercell of 54-x water molecules and x={1,2,4,6} LiCl pairs disposed following the experimental structure indicated in ref. 37, to elucidate the effect of salt inclusion in ice lattice on the H-bond symmetrization (for details, see *Methods*).

To estimate the ice VII to ice X transition, we calculated the H–O first and second neighbors distributions along our ab initio molecular dynamics (MD) simulations. When the system is ice VII-like, this distribution is double-peaked; at the transition pressure, the system becomes ice X-like, i.e., the hydrogen atoms occupy the symmetric position along the O–O directions and the above distributions merge and can be fitted at comparable quality by a single-peaked function.

We report in Fig. 4 the main result of our experimental and computational study: The inclusion of ions pushes the ice VII to ice X to higher and higher pressures, and this occurs with a nearly exponential law, with a similar trend observed both from experiment and simulations. The shift of almost 35 GPa between the ab initio calculations and the experimental transition, defined by the appearance of the T_{2g} Raman mode, is likely due to quantum effects, and, in particular, to the fact that nuclei are approximated as classical particles in our ab initio molecular dynamics calculations, and are therefore unable to tunnel through the potential barrier (31). Moreover, our classical description of nuclei hinders a finer description of possible isotopic effects (32). A deeper atomic-level analysis reveals that the bond symmetrization is indeed hindered by the ions, particularly in the first neighbor shell of an ionic intrusion (see Fig. 4, *Inset*). Similar results have been obtained for NaCl solutions close to the eutectic composition ($R = 11.5$), where no appearance of the T_{2g} mode has been observed up to 1.5 Mbar pressure.

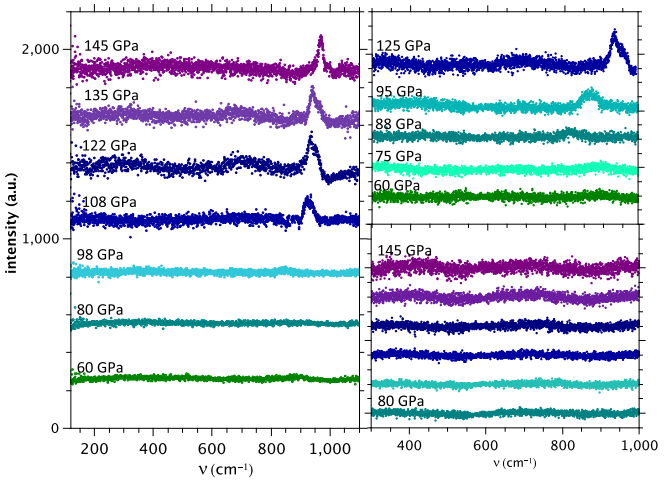

Fig. 3. High-resolution Raman scattering measurements in the 300–1,000 cm^{-1} range as a function of pressure up to 150 GPa for $R = 50$ (*Top Right*), $R = 30$ (*Left*), and $R = 6$ (*Bottom Right*) water molecules for LiCl. Numbers indicate the nominal pressure in GPa. The transition from ice VII to ice X phase is observed by the appearing of the T_{2g}O vibrational mode.

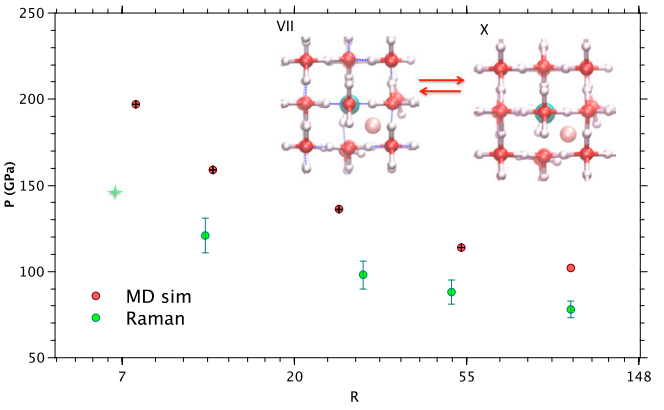

Fig. 4. Ice VII to ice X transition pressure dependence on salt concentration in LiCl:RH_2O solutions as measured by Raman scattering experiments (green dots) and calculated by ab initio simulations (red dots). The green cross represents the maximum pressure value reached for the LiCl:$6H_2O$ sample where the transition has not been observed. Simulation snapshots of the ice X phase in pure water and LiCl:$20H_2O$ are shown. No symmetrization of the bond occurs near the ion impurity.

We attribute this effect to the strong local perturbation introduced by the charged ion. In fact, in pure ice, the bond symmetrization seems to occur as a synchronized displacement of all hydrogen atoms, which are all topologically identical; conversely, in salty ices, this topological invariance is lost, hydrogens are different according to their proximity to salt's anions or cations, and this also constrains the water molecules orientational degrees of freedom.

Ice X is thought to be the precursor for a superionic ice phase (33, 34), which would manifest in the pressure range of ice X but at higher temperatures. The superionic phase is a nonmolecular phase characterized by mobile delocalized hydrogen atoms moving in the oxygen lattice and giving rise to electrical conduction. This ice phase is thought to be the dominant phase of the interior of giant icy planets and may be responsible for the observed anomalous magnetic moment of Uranus and Neptune. Recent studies showed experimental evidence for superionic conduction at significantly low temperature compared with earlier theoretical estimates (17, 18, 50). The presence of salt impurities in natural ice, incorporated via ocean–ice interaction, rock–ice interaction at depth, or processes that occurred during accretion (1, 2, 23–25), could strongly modify the thermodynamic conditions and the mechanism for the appearance of change in such an extreme state of matter, and eventually promote novel exotic properties, thus challenging our present description of the physics of these bodies, essentially based on the assumption of the properties of pure ice under high pressure. We believe that the ionic impurity effects on the onset of superionicity and on the high-pressure phases predicted in ice strongly demand systematic investigation.

Methods

Sample Preparation. Salty ice VII samples were produced following the procedure described in refs. 37–39. by $R = 6$ aqueous solutions loaded into high-pressure chambers of 30–40 μm in diameter in a rhenium gasket between two type IIa synthetic diamonds mounted on a symmetric Mao–Bell-type cell. A salt-doped amorphous sample was produced by hyperquenching $R = 12$ aqueous solution (39), loaded under liquid nitrogen, compressed to 4 GPa, and then annealed at this pressure, to promote salt inclusion in the ice lattice (37). Finally, $R = 30$ and $R = 50$ LiCl aqueous solutions were loaded in the cell at ambient temperature and compressed to 5 GPa, warmed at 400 °C, and then quenched to 77 K by immersing the cell in liquid nitrogen.

As previously observed, the open structure phases of ice, like Ice Ih, Ic, and IX, expel salt from their lattice when they nucleate, so that, at low pressure, salty ice exists only in its high-density amorphous phase (s-HDA) (38, 39, 49),

which transforms under compression to a very high-density phase (s-VHDA) octahedrally coordinated around Li ions. When annealed at room temperature under high pressure, this s-VHDA transforms into a salty ice VII structure, including the Li ion as interstitial and the Cl ion as substitutional inclusion (37). The proton-ordered ice VIII phase is, conversely, suppressed by the presence of salt that disorients the water molecules network.

High-Pressure Raman Scattering. Raman scattering measurements were performed on an HR800 commercial confocal Raman spectrometer equipped with Cobolt 532-nm 2-W DPSS laser. We used a long working distance 50× Mitutoyo objective.

Owing to the very low scattering cross section of the H_2O at these pressures, careful measurements of the background luminescence and Raman scattering from the diamond anvils were conducted. We used high-purity ultralow-fluorescence diamond anvils in a confocal optical configuration with a tightly focused laser that substantially suppresses the luminescence and spurious Raman signals. Furthermore, at each pressure point, we measured the scattered signal from the stressed diamond anvil in contact with the gasket, close to the gasket–sample boundary, and we evaluated the pressure gradient due to the shear strength of ice by measuring the pressure, via the ruby fluorescence, at different points of the sample area. The pressure gradient increased from 0.2 GPa to 0.3 GPa at 3–4 GPa up to 3 GPa at 60 GPa.

For each pressure point, spectra were collected with low [600 lines per millimeter (l/mm) grating] and high (1,800 l/mm grating) spectral resolution modes. The first mode was used for recording very broad spectral features in the 500–4,500 cm^{-1} range, whereas the second provided more accurate measurement of the narrow bands, and was mainly used in the 100–1,200 cm^{-1} range.

Spectra along the 295 K isotherm were systematically measured by increasing and decreasing pressure conditions, to test the reproducibility of the results.

Representative Raman spectra and background subtraction for 15 mol% solution, 5 mol% solution, and pure water in the high-frequency range are shown in *Supporting Information*.

Ab Initio Molecular Dynamics Simulations. Density functional theory (DFT) calculations were, at first, performed on a $3 \times 3 \times 3$ supercell of pure ice VII (54 water molecules) using the CASTEP Code (51). All calculations were then repeated with salty ice with the same cell containing *54-x* water molecules and *x={1,2,4,6}* LiCl pairs. Li and Cl ions were distributed using a random number generator, to replace random water molecules of the ice lattices with Cl ions at the oxygen position, and to place Li ions at a random interstitial position, namely the face centers of the notional one-molecule ice VII unit cell following the experimental structure indicated in ref. 37. Best configurations were chosen based on the lowest energies and most uniform distribution of ions within the lattice.

The first part of the theoretical work involved static structural relaxations to determine the optimal settings for the ab initio molecular dynamics simulations, establish the nature of the phase transition for pure and salty ice, and estimate a pressure for the transition.

Proton-disordered configurations were obtained using the following procedure: An ordered ice VII cell was set up (not necessarily obeying the ice rules). The oxygen positions were fixed, and classical isochoric-isothermal (NVT) molecular dynamics was run at high temperatures (2,000 K) using the TIP4P/2005 rigid body empirical potential, randomizing the molecular orientations. The system was then gradually quenched to vanishing temperature, and the final configurations were taken. These configurations were validated against violations of the ice rules and used as the starting points for subsequent ab initio ice VII calculations. The energy differences between different proton-ordered configurations are minimal, as little as 1 meV per atom (52), and are minimal compared with the defect energy caused by introducing Li and Cl ions into the lattice.

The PBE exchange correlation functional was used with a plain wave cutoff of 380 eV, and the Brillouin zone was sampled at the gamma point only. Calculations were considered to be converged when the energy changed by less than 10^{-6} eV between steps. Convergence thresholds of 10^{-5} eV for the energy, 2×10^{-3} Å for ionic displacements and 5×10^{-2} eV/Å for forces were used in the geometry optimization. The cell parameter of the supercell was varied in decrements of 0.01 Å, the ionic positions were relaxed until the forces were minimized, and the hydrostatic pressure was calculated.

This process was repeated using isobaric–isothermal (NPT) ab initio molecular dynamics simulations with the same supercell at 300 K and a range of pressures and concentrations. Identical electronic structure calculation parameters were used as for the static DFT calculations. A timestep of 1 fs was used, with a Nosé–Hoover thermostat with a 0.1-ps time period and an Andersen–Hoover barostat with a 0.5-ps period.

At the highest pressure, the ice X structure was used as the initial configuration. Then NPT ab initio molecular dynamics was started, equilibrating the system for 1–2 ps and collecting statistics for 10–60 ps. The final configuration of this run was then equilibrated at the next lowest pressure, then the simulation was run for 10–60 ps, and so on, until the lowest pressure was reached. OH and H bond lengths were sampled every 10 fs for 10 ps. The transition pressure was estimated as the pressure to which calculated H–O first and second neighbors distributions can be fitted at comparable quality by a single-peaked function.

This procedure actually does not show any hysteresis, which is consistent with the static calculations, showing that the enthalpy varies smoothly as a function of pressure, with no discontinuity that would indicate a first-order transition.

ACKNOWLEDGMENTS. This work was supported by the Swiss National Science Foundation through FNS Grant 200021-149847 and by the French state funds managed by ANR within the Blanc International programme PACS under reference ANR-13-IS04-0006-01 and the Investissements d'Avenir programme under reference ANR-11-IDEX-0004-02, and more specifically within the framework of the Cluster of Excellence MATériaux Interfaces Surfaces Environnement (MATISSE) led by Sorbonne Universites. Z.R. and A.M.S. acknowledge the Grand Equipement National de Calcul Intensif French National Supercomputing Facility (Project Grants x2013091387 and following), and the Swedish National Infrastructure for Computing National Supercomputing Centre for computing resources.

1. De Pater I, Lissauer JJ (2004) *Planetary Sciences* (Cambridge Univ Press, Cambridge, UK).
2. Guillot T (1999) Interiors of giant planets inside and outside the solar system. *Science* 286(5437):72–77.
3. Kuhs WF, Finney JL, Vettier C, Bliss DV (1984) Structure and hydrogen ordering in ices VI, VII and VIII by neutron powder diffraction. *J Chem Phys* 81(8):3612–3623.
4. Nelmes RJ, et al. (1998) Multisite disordered structure of ice VII to 20 GPa. *Phys Rev Lett* 81(13):2719–2722.
5. Goncharov AF, Struzhkin VV, Somayazulu MS, Hemley RJ, Mao HK (1996) Compression of ice to 210 Gigapascals: Infrared evidence for a symmetric hydrogen-bonded phase. *Science* 273(5272):218–220.
6. Goncharov AF, Struzhkin VV, Mao HK, Hemley RJ (1999) Raman spectroscopy of dense H_2O and the transition to symmetric hydrogen bonds. *Phys Rev Lett* 83(10):1998–2001.
7. Pruzan Ph (1994) Pressure effects on the hydrogen bond in ice up to 80 GPa. *J Mol Struct* 322(1-2):279–286.
8. Loybeyre P, LeToullec R, Wolanin E, Hanfland M, Hausermann D (1999) Modulated phases and proton centring in ice observed by X-ray diffraction up to 170 GPa. *Nature* 397(6719):503–506.
9. Aoki K, Yamawaki H, Sakashita M, Fujihisa H (1996) Infrared absorption study of the hydrogen-bond symmetrization in ice to 110 GPa. *Phys Rev B Condens Matter* 54(22): 15673–15677.
10. Sugimura E, et al. (2008) Compression of H_2O ice to 126 GPa and implications for hydrogen-bond symmetrization: Synchrotron x-ray diffraction measurements and density-functional calculations. *Phys Rev B* 77(21):214103.
11. Guthrie M, et al. (2014) Neutron diffraction observations of interstitial protons in dense ice. *Proc Natl Acad Sci USA* 110(26):10552–10556.
12. Hemley RJ (2000) Effects of high pressure on molecules. *Annu Rev Phys Chem* 51: 763–800.
13. Loubeyre P, et al. (1996) X-ray diffraction and equation of state of hydrogen at megabar pressures. *Nature* 383(6602):702–704.
14. Goncharov AF, Gregoryanz E, Hemley RJ, Mao H (2001) Spectroscopic studies of the vibrational and electronic properties of solid hydrogen to 285 GPa. *Proc Natl Acad Sci USA* 98(25):14234–14237.
15. Zha CS, Cohen RE, Mao HK, Hemley RJ (2014) Raman measurements of phase transitions in dense solid hydrogen and deuterium to 325 GPa. *Proc Natl Acad Sci USA* 111(13):4792–4797.
16. Datchi F, et al. (2006) Solid ammonia at high pressure: A single-crystal x-ray diffraction study to 123 GPa. *Phys Rev B* 73(17):174111.
17. Ninet S, et al. (2013) Experimental and theoretical evidence for an ionic crystal of ammonia at high pressure. *Phys Rev B* 89(17):174103.
18. Ninet S, Datchi F, Saitta AM (2012) Proton disorder and superionicity in hot dense ammonia ice. *Phys Rev Lett* 108(16):165702.
19. Hirai H, Konagai K, Kawamura T, Yamamoto Y, Yagi T (2008) Solid methane behaviours under high pressure at room temperature. *J Phys Conf Ser* 121(10):102001.
20. Katayama Y, Hattori T, Saitoh H, Ikeda T, Aoki K (2010) Structural and dynamical properties of water under high temperatures and pressures. *Phys Rev B* 81(1):014109.
21. Saitta AM, Datchi F (2003) Structure and phase diagram of high-density water: The role of interstitial molecules. *Phys Rev E Stat Nonlin Soft Matter Phys* 67(2 Pt 1):020201.
22. Goncharov AF, et al. (2005) Dynamic ionization of water under extreme conditions. *Phys Rev Lett* 94(12):125508.
23. Anderson JD, et al. (1998) Europa's differentiated internal structure: Inferences from four Galileo encounters. *Science* 281(5385):2019–2022.

24. Schilling N, Khurana KK, Kivelson MG (2004) Limits on an intrinsic dipole moment in Europa. *J Geophys Res* 109(E5):E05006.
25. Khurana KK, et al. (1998) Induced magnetic fields as evidence for subsurface oceans in Europa and Callisto. *Nature* 395(6704):777–780.
26. Lissauer JJ (2002) Extrasolar planets. *Nature* 419(6905):355–358.
27. Benoit M, Marx D (2005) The shapes of protons in hydrogen bonds depend on the bond length. *ChemPhysChem* 6(9):1738–1741.
28. Benoit M, Bernasconi M, Focher P, Parrinello M (1996) New high-pressure phase of ice. *Phys Rev Lett* 76(16):2934–2936.
29. Benoit M, Marx D, Parrinello M (1998) Tunnelling and zero-point motion in high-pressure ice. *Nature* 392(6673):258–261.
30. Caracas R (2008) Dynamical instabilities of ice X. *Phys Rev Lett* 101(8):085502.
31. Bronstein Y, Depondt P, Finocchi F, Saitta AM (2014) Quantum-driven phase transition in ice described via an efficient Langevin approach. *Phys Rev B* 89(21):214101.
32. Hermann A, Ashcroft NW, Hoffmann R (2013) Isotopic differentiation and sublattice melting in dense dynamic ice. *Phys Rev B* 88(21):214113.
33. Cavazzoni C, et al. (1999) Superionic and metallic states of water and ammonia at giant planet conditions. *Science* 283(5398):44–46.
34. Wilson HF, Wong ML, Militzer B (2013) Superionic to superionic phase change in water: Consequences for the interiors of Uranus and Neptune. *Phys Rev Lett* 110(15): 151102.
35. Schweizer KS, Stillinger FH (1984) High pressure phase transitions and hydrogen-bond symmetry in ice polymorphs. *J Chem Phys* 80(3):1230–1240.
36. Klimeš J, Bowler DR, Michaelides A (2013) Understanding the role of ions and water molecules in the NaCl dissolution process. *J Chem Phys* 139(23):234702.
37. Klotz S, Bove LE, Strässle T, Hansen TC, Saitta AM (2009) The preparation and structure of salty ice VII under pressure. *Nat Mater* 8(5):405–409.
38. Bove LE, Klotz S, Philippe J, Saitta AM (2011) Pressure-induced polyamorphism in salty water. *Phys Rev Lett* 106(12):125701.
39. Ludl AA, et al. (2015) Structural characterization of eutectic aqueous NaCl solutions under variable temperature and pressure conditions. *Phys Chem Chem Phys* 17(21): 14054–14063.
40. Frank MR, et al. (2006) Experimental Study of the NaCl–H_2O system up to 28GPa: Implications for ice-rich planetary bodies. *Phys Earth Planet Inter* 155(1-2):152–162.
41. Frank MR, Aarestad E, Scott HP, Prakapenka VB (2013) A comparison of ice VII formed in the H_2O, NaCl-H_2O, and CH_3OH-H_2O systems: Implications for H_2O-rich planets. *Phys Earth Planet Inter* 215:12–20.
42. Journaux B, et al. (2013) Influence of NaCl on ice VI and ice VII melting curves up to 6 GPa, implications for large icy moons. *Icarus* 226(1):355–363.
43. Lokshin KA, et al. (2004) Structure and dynamics of hydrogen molecules in the novel clathrate hydrate by high pressure neutron diffraction. *Phys Rev Lett* 93(12):125503.
44. Loveday JS, Nelmes RJ (2008) High-pressure gas hydrates. *Phys Chem Chem Phys* 10(7): 937–950.
45. Takii Y, Koga K, Tanaka H (2008) A plastic phase of water from computer simulation. *J Chem Phys* 128(20):204501.
46. Aragones JL, Vega C (2009) Plastic crystal phases of simple water models. *J Chem Phys* 130(24):244504.
47. Angell CA, Sare E (1970) Glass-forming composition regions and glass transition temperatures for aqueous electrolyte solutions. *J Chem Phys* 52(3):1058–1068.
48. Kanno H, Angell CA (1977) Homogeneous nucleation and glass formation in aqueous alkali halide solutions at high pressure. *J Phys Chem* 81(26):2639–2643.
49. Ruiz GN, Bove LE, Corti HR, Loerting T (2014) Pressure-induced transformations in LiCl-H_2O at 77 K. *Phys Chem Chem Phys* 16(34):18553–18562.
50. Sugimura E, et al. (2012) Experimental evidence of superionic conduction in H_2O ice. *J Chem Phys* 137(19):194505.
51. Clark SJ, et al. (2005) First principles methods using CASTEP. *Z Kristallogr* 220:567–570.
52. Raza Z, et al. (2011) Proton ordering in cubic ice and hexagonal ice; a potential new ice phase—XIc. *Phys Chem Chem Phys* 13(44):19788–19795.